ADVANCED MATERIALS INTERFACES
www.advmatinterfaces.de

Optical Coherence Tomography of Van Der Waals Heterostructures Using Extreme Ultraviolet Light

Felix Wiesner, Johann J. Abel, Muhammad Hussain, Vipin Krishna, Alisson R. Cadore, Juan P. G. Felipe, Ana M. Valencia, Martin Wünsche, Julius Reinhard, Marco Gruenewald, Caterina Cocchi, Gerhard G. Paulus,* Giancarlo Soavi,* and Silvio Fuchs**

New experimental methods with high out-of-plane spatial sensitivity combined with ultrafast temporal resolution can revolutionize the understanding of charge- and heat-transfer dynamics occurring at interfaces. In this work, a step forward is taken in this direction by applying coherence tomography with extreme ultraviolet (EUV) light to different van der Waals heterostructures, which enables a 3D sample reconstruction with nanoscopic axial resolution. Furthermore, the measurements and, more in general, the approach is confirmed by ab initio calculations of the refractive index of layered materials that we compare to existing databases of empirical data. The EUV coherence tomography contrast is estimated in a broad spectral range (photon energy 65 –100 eV). This work sets the basis for the development of a new spectroscopy tool that, thanks to the temporal profile of EUV light sources and the high axial resolution of coherence tomography, can become the ideal probe of ultrafast processes occurring in van der Waals heterostructures and buried nanoscale opto-electronic devices.

1. Introduction

Layered materials (LMs) such as graphene, transition-metal dichalcogenides (TMDs), hexagonal boron nitride (hBN), and layered magnets are essential building blocks for the next generation of electronic, spintronic, opto-electronic, and photonic devices. These include, for instance, nanoscale field effect transistors (FETs)[1] and spin FETs,[2] ultrafast logic gates,[3,4] integrated nanophotonic circuits,[5] ultrafast light-emitting diodes[6] and photodetectors.[7] A further distinctive advantage of LMs is the possibility of stacking them with exquisite control and precision into van der Waals heterostructures (vdW-HS).[8] As a matter of fact, vdW-HS represents the gold standard for realizing high-quality encapsulated devices, such as high-mobility graphene FETs[9] and high-speed graphene detectors.[10] At the same time, vdW-HS are emerging as the ideal playground for exploring new exotic phenomena in condensed matter physics, such as unconventional superconductivity in twisted bilayer graphene[11] or moiré excitons in bilayer TMDs.[12] In both contexts, interlayer interactions and interface processes play a key role. For instance: 1)

F. Wiesner, J. J. Abel, M. Wünsche, J. Reinhard, G. G. Paulus, S. Fuchs
Institute of Optics and Quantum Electronics
Friedrich Schiller University Jena
Max-Wien-Platz 1, 07743 Jena, Germany
E-mail: gerhard.paulus@uni-jena.de; silvio.fuchs@uni-jena.de

M. Hussain, V. Krishna, M. Gruenewald, G. Soavi
Institute of Solid State Physics
Friedrich Schiller University Jena
Helmholtzweg 5, 07743 Jena, Germany
E-mail: giancarlo.soavi@uni-jena.de

A. R. Cadore
Brazilian Nanotechnology National Laboratory (LNNano)
Brazilian Center for Research in Energy and Materials (CNPEM)
Campinas–SP 13083-100, Brazil

The ORCID identification number(s) for the author(s) of this article can be found under https://doi.org/10.1002/admi.202400534

DOI: 10.1002/admi.202400534

J. P. G. Felipe, A. M. Valencia, C. Cocchi
Physics Department and IRIS Adlershof
Humboldt-Universität zu Berlin
12489 Berlin, Germany
E-mail: caterina.cocchi@uni-oldenburg.de

J. P. G. Felipe
Department of Physics
Freie Universität Berlin
14195 Berlin, Germany

A. M. Valencia, C. Cocchi
Institute of Physics
Carl-von-Ossietzy Universität Oldenburg
26129 Oldenburg, Germany

M. Wünsche, G. G. Paulus, S. Fuchs
Helmholtz Institute Jena
GSI Helmholtzzentrum für Schwerionenforschung GmbH
Fraunhofer Str. 8, 07743 Jena, Germany

M. Wünsche
Indigo Optical Systems GmbH
Moritz-von-Rohr-Str. 1a, 07745 Jena, Germany

S. Fuchs
Laserinstitut Hochschule Mittweida
University of Applied Science Mittweida
Technikumplatz 17, 09648 Mittweida, Germany

The twist angle in vdW-HS that is based on magnetic LMs could be used to engineer time-reversal asymmetry and non-uniform spin textures;[2] 2) Interlayer charge transfer occurring faster than internal recombination enables hot electron transfer for photovoltaic applications beyond the Shockley–Queisser limit;[13] 3) The coupling between hot electrons in graphene and hBN hyperbolic phonons allows out-of-plane heat dissipation and engineered thermal management.[14]

Direct and noninvasive imaging of interfaces, combined with high temporal resolution, can provide new insights into the dynamical processes occurring in vdW-HS, with huge benefits for science and technology. However, the current methods to characterize vdW-HS have limited capabilities in this regard. Optical techniques such as Raman spectroscopy,[15–17] visible-light microscopy,[18] nonlinear optical effects,[19] or time-resolved absorption and photocurrent measurements[20] lack out-of-plane sensitivity. In contrast, time-resolved X-ray spectroscopy[21] at large-scale synchrotron facilities provides high axial resolution but limited temporal resolution (tens of picoseconds), which is insufficient to study the ultrafast interlayer dynamics of vdW-HS.

Here, we introduce a new approach based on optical coherence tomography with extreme ultraviolet light (XCT)[22–24] that can potentially combine nondestructive high spatial (axial) and temporal resolution. The use of extreme ultraviolet (EUV) light for time-resolved measurements is gaining interest thanks to the recent improvement of coherent EUV sources powered by high-power short-pulse lasers.[25,26] The generation mechanism of EUV, namely high-harmonic generation (HHG),[27–29] is the basis of attosecond science,[30] as the generated harmonics of the driving laser frequency are emitted in bursts of attosecond pulses or even of isolated pulses. The technique was awarded the Nobel Prize in Physics in 2023. Even in case the attosecond regime is not reached, transient measurement with HHG sources can provide few-femtosecond temporal resolution. Transient absorption and reflectivity measurements in the EUV are highly sensitive to electronic effects in the vicinity of core-level transitions.[31–33]

Beyond ultrafast spectroscopy, imaging with EUV light from HHG sources has made remarkable progress in recent years.[34] The wavelength of EUV is roughly 10–15 times shorter than that of visible light, leading to improved resolutions. Depending on the material, EUV attenuation lengths can be up to a few µm, which enables imaging internal structures in nanodevices. Transmission lengths in the micrometer range, on the other hand, restrict the use of transmissive optics. For this reason, lensless techniques, such as coherent diffraction imaging or ptychography,[35–37] or diffraction-based techniques, such as Fresnel zone plates,[38] have been used to achieve lateral resolution of the order of a few tenths of nanometers.[39,40] Due to the low photon flux in laboratory EUV experiments and the lack of destructive sample preparation such as slicing, these techniques enable non-destructive sample characterization.[34,41] However, these methods largely lack the desired axial sensitivity and have not been used for imaging of vdW-HS so far. In contrast, XCT is a broadband EUV imaging technique that features ultrahigh axial sensitivity and resolution, as we have recently shown by imaging monolayers of graphene embedded in silicon.[42]

In this work, we use our XCT approach to image a $MoTe_2$-hBN-vdW-HS and we study the contrast and resolution of the technique for different combinations of LMs. In addition, we compare the semiempirical database values for the refractive index in the EUV to ab initio calculations for LMs. Thus, this work sets the basis for the development of a new spectroscopy and imaging method for LMs: owing to the temporal profile of the EUV light sources and the high axial resolution of XCT, time-dependent XCT can become a powerful probe of vdW-HS and buried nanoscale opto-electronic devices.

2. Results and Discussion

2.1. Optical Coherence Tomography with Extreme Ultraviolet Light

Figure 1a shows the principle of XCT. The sample is illuminated with broadband EUV light, which is partially reflected at the sample interfaces. The reflected beams from the different interfaces interfere and lead to modulations in the reflected spectrum, which are detected by a spectrometer. A Fourier transform-based reconstruction[22,24] yields the depth structure of the sample, as shown in Figure 1b,c. Note that the direct Fourier transform as used here will only yield the autocorrelation of the light reflected from the sample. To obtain the sample structure, which differs significantly from the autocorrelation in the case of complex vdW-HS, a phase reconstruction must be performed, as discussed in refs. [22,24].

The depth resolution of XCT is determined by the width $\Delta\lambda$ and the central wavelength λ of the EUV spectrum:

$$\delta_z \sim \lambda^2/\Delta\lambda \tag{1}$$

In ref. [43] an EUV spectrum with photon energies $E = 36 - 98$ eV has been used to produce an axial resolution of 16 nm[43] at 15° angle of incidence. However, axial features with thicknesses far below this value can be detected, if there is a sufficiently large change in the refractive index. In this case, the axial accuracy of XCT can reach at least 4 nm.[22] In addition, even sub-nanometer thicknesses can be recovered by utilizing model-based approaches.[42]

The lateral information is retrieved by repeating the measurement at different positions on the sample. Consequently, the lateral resolution is determined by the spot size of the EUV beam on the sample. In this work, we used a spot size of ≈25 µm, obtained by focusing the EUV radiation with a toroidal mirror. However, we stress this lateral resolution in the few nanometer range has been obtained with lensless EUV imaging techniques[34] and progress in EUV and X-ray focussing will enable increased lateral resolution.[44,45] In each lateral position, the broadband spectrum is measured and used for the reconstruction of the depth structure. This finally gives a 3D image of the sample, as shown in Figure 1d. For each lateral point, the XCT image yields the position of internal features with respect to the surface of the sample. Note that the topography of the sample's surface is not measured in XCT, but some basic assumptions allow to correctly align the 3D structure. For instance, for the simulation displayed in Figure 1d the presence of a flat substrate is sufficient to align the XCT image, and the effect of absorption inside the sample manifests as a shadow of the vdW-HS on the substrate.

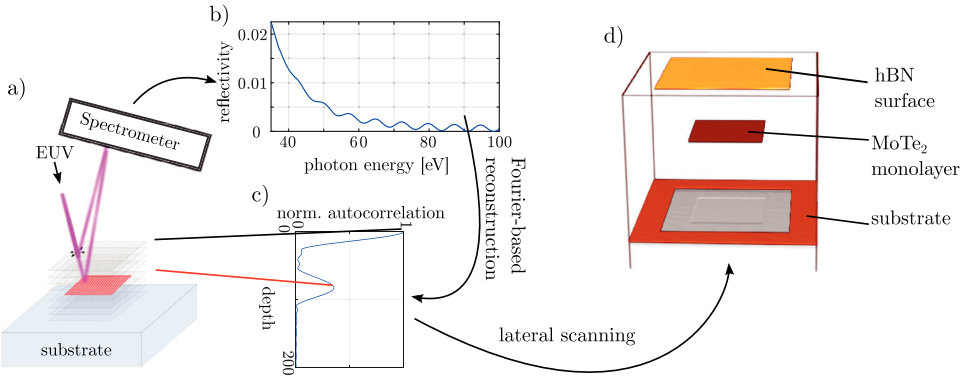

Figure 1. Schematic representation of the principles of EUV coherence tomography on vdW-HS: a) A vdW-HS is illuminated with EUV radiation. b) Interference from different layers causes modulation in the reflected spectrum. c) These modulations can be used to compute the axial structure of the vdW-HS. As an example, the reconstruction of the simulated reflectivity of a $MoTe_2$ monolayer in hBN is shown (solid line). d) The measurement is repeated at different lateral positions to obtain the 3D sample structure.

2.2. Imaging of $MoTe_2$ in hBN

We start by showing results of XCT imaging a vdW-HS consisting of a $MoTe_2$ monolayer encapsulated by two bulk hBN (top and bottom) flakes. **Figure** 2a) shows the optical image of the investigated sample. A 3D sketch of the sample structure obtained by combining results from XCT, atomic force microscopy (AFM) and visible microscopy is shown in Figure 2b. Detailed results of the AFM measurements are shown in the Supporting Information. The top upper flake (red-shaded in Figure 2b) is larger than the lower one (gray). Consequently, there are two regions (A and C) in which the top hBN flake lies

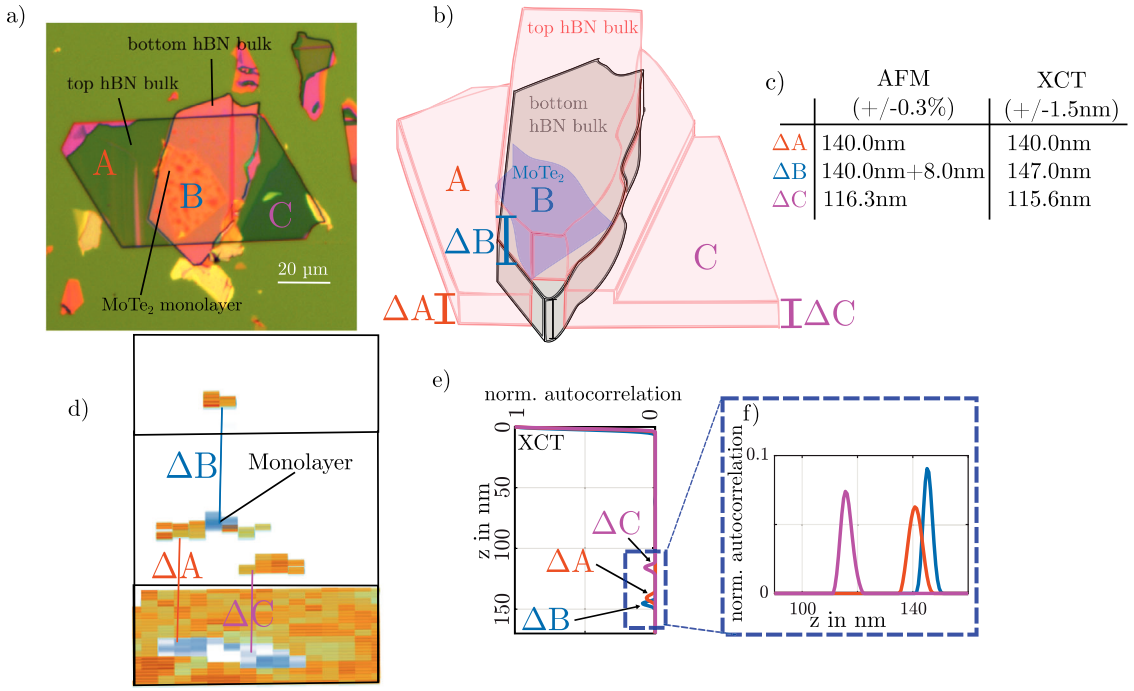

Figure 2. Characterization of a hBN-$MoTe_2$-vdW-HS: a) Visible microscopy image of the sample b) Combining information from visible microscopy, AFM (see Supporting Information) and XCT, we generated a 3D sketch of the sample. The upper (red) hBN flake is larger than the lower (black) flake. Therefore in regions A and C the upper hBN flake forms an interface with the substrate. In region B the $MoTe_2$ monolayer is encapsulated between two hBN flakes. AFM measurements at the edges of the bulk are used to characterize their thickness. c) AFM measurements are compared to the XCT measurements. d) In the 3D XCT reconstruction, the encapsulated $MoTe_2$ monolayer can be clearly resolved. The XCT measurements at different lateral positions are aligned to match the sample topology. e,f) Comparison of the XCT depth structure from the three regions A, B, and C. As expected from the AFM measurements, we measure a difference in thickness in the regions A and C. In addition, the top hBN layer is found to be thicker above the monolayer in region B compared to region A. AFM measurements (see Supporting Information) confirm a step of ≈ 8 nm in the hBN surface above the monolayer due to transfer residues or trapped molecules.[46]

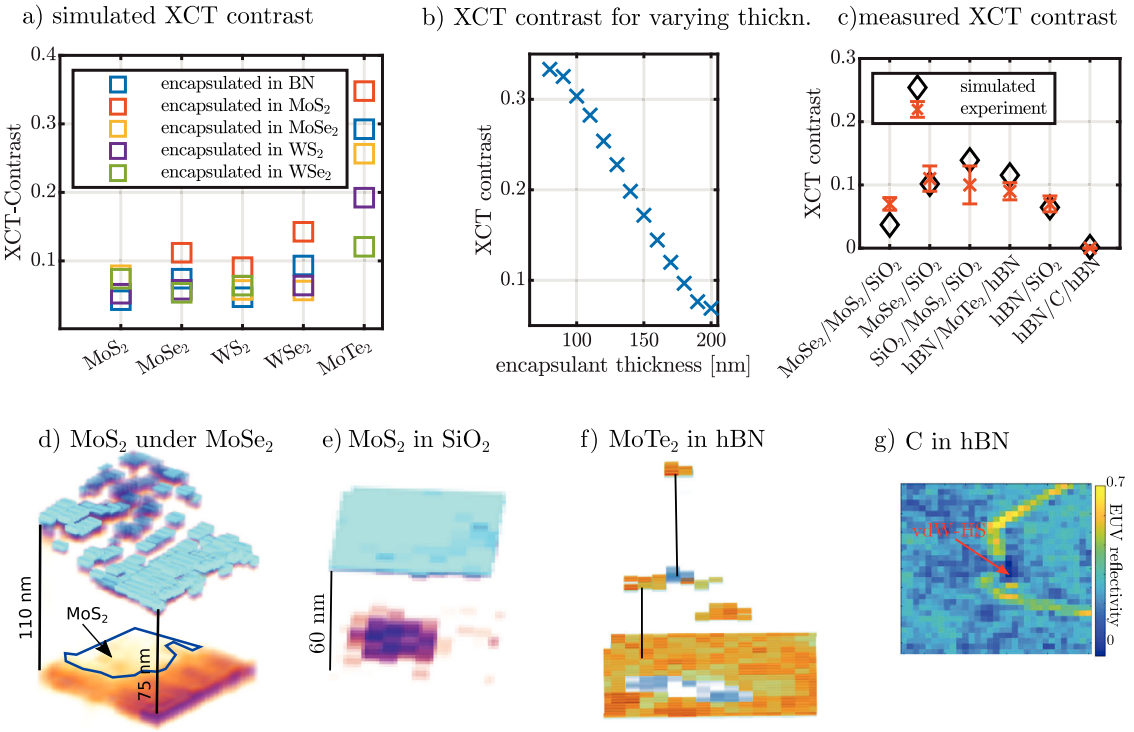

Figure 3. XCT contrast of different vdW-HS: a) The XCT contrast is simulated for varying encapsulant and monolayer materials. b) The XCT contrast was simulated for varying thicknesses of the top flake in a hBN-$MoTe_2$ vdW-HS. c) Experiments on different samples were performed to compare predicted and measured contrasts. The reconstructions of the respective samples are shown in the following figures: d) XCT reconstruction of a $MoS_2/MoSe_2$ vdW-HS e) XCT reconstruction of MoS_2 in SiO_2 f) XCT reconstruction of $MoTe_2$ in hBN (detailed in Figure 2) g) EUV reflectivity scan of C in hBN (no XCT contrast, no XCT reconstruction possible).

directly on the substrate. In between is the region of the $MoTe_2$ monolayer between two hBN layers (B). The XCT image of the sample is shown in Figure 2d and the depth structure from the regions A, B, and C are shown in Figure 2e,f. The depth axis in the lateral sample positions was aligned to the sample topography.

In regions A and C, XCT can be used to characterize the thickness ΔA and ΔC of the top hBN on the substrate. The top layer is thinner in region C than in region A ($\Delta C < \Delta A$, yellow and red in Figure 2e). In region B, we measure a strong signal caused by the encapsulated monolayer. AFM at the edges of the samples can be used to verify the XCT measurement of the thicknesses ΔA and ΔC.

In region B, the XCT shows a thickness of 7 ± 1.5 nm larger than the hBN flake. This is again confirmed by AFM measurements (see Supporting Information), which show a step height of ≈8 nm on the sample surface above the monolayer. This means that the $MoTe_2$ monolayer appears considerably thicker than the expected ≈0.7 nm.[47] Most likely this is due to residual material from the transfer process or trapped molecules[46] between hBN and $MoTe_2$.

In this section, we used AFM to complement the information obtained by XCT and to validate some of the results. It is important to highlight that while AFM is highly complementary to XCT and partially provides similar information, only the latter can truly image the subsurface structure of the sample, because the XCT signal is created by light reflected from the encapsulated monolayer interfering with light reflected from the sample surface.

2.3. XCT Measurements in Different vdW-HS

Our XCT measurement of a $MoTe_2$ monolayer encapsulated by two hBN flakes demonstrates the potentials of XCT, and EUV imaging in general, for the study of vdW-HS. Next, we investigate the applicability of the method to vdW-Hs of different LMs. We calculate the refractive index of the LM's from the tabulated values for the atomic scattering factors of the elements[48] and estimate the XCT contrast for different vdW-HS.

The expected contrasts for XCT measurements of different vdW-HS in the spectral range from $E = 65$ eV to $E = 100$ eV are shown in **Figure 3a**. Calculations were performed for vdW-HS with a thickness of the top encapsulant of 80 nm. Depending on the encapsulant bulk material and the encapsulated monolayer material, we observe large differences in the simulated XCT contrast. These are caused by the strongly material-specific absorption in the bulk materials and varying reflectivity of the bulk-monolayer interfaces. In particular, $MoTe_2$ monolayers show a very high contrast for almost all encapsulant materials.

In addition to the dependence of the contrast on the materials, the contrast is also strongly influenced by the

structure of the vdW-HS. Figure 3b shows a simulation of a hBN-$MoTe_2$ similar to the one investigated in Figure 2 for different thicknesses of the top hBN flake. The contrast is found to decrease significantly with increasing thickness of the top encapsulant. For this particular sample, encapsulant thicknesses below 180 nm yield very favorable contrasts above 0.1.

To validate our simulations, we measured the XCT images of different vdW-HS, as shown in Figure 3c–g. The measured XCT contrasts are compared to the simulations based on the database in ref. [48], as reported in Figure 3c. Different types of sample architecture were investigated: 1) a MoS_2 monolayer directly placed on a SiO_2 substrate and covered with $MoSe_2$ bulk (Figure 3d), 2) MoS_2 encapsulated in SiO_2 (Figure 3e), 3) the hBN-$MoTe_2$ vdW-HS already discussed in detail in this work (Figure 3f), and 4) a graphene-hBN vdW-HS (Figure 3g).

We conclude that, with the exception of graphene encapsulated in hBN, all vdW-HS can be characterized using XCT. Furthermore, the measured contrast is in reasonable agreement with contrast simulations using the scattering factors from ref. [48]. Note that the sample preparation yielded strongly varying encapsulant thicknesses, which was taken into account in the simulations. Deviations between simulated and measured contrasts can be caused by sample imperfections or deviations in the tabulated scattering factors. In the case of the hBN-C-vdW-HS, the low contrast is also correctly predicted by the contrast estimation. it is caused by an encapsulant thickness of 250 nm and a low difference in refractive index between the two LMs. Higher contrasts can be expected for thinner samples and different spectral ranges of the measurement. Furthermore the EUV reflectivity of vdW-HS is expected to decrease with increasing interface roughness.[49] Previous work on metallic layer systems[50] yielded detection limits of 5 nm RMS roughness.

2.4. Refractive Index of LMs in the Extreme Ultraviolet Spectral Range and Simulation of the XCT Contrast

Our experimental results demonstrate the feasibility of nondestructive characterization of LMs and vdW-HS with XCT. In addition, we showed that the semiempirical scattering factors from ref. [48] can be used to estimate the XCT contrast in future experiments. However, for the investigation of electronic and time-dependent effects in vdW-HS and LMs a more sophisticated understanding of the interaction with EUV becomes necessary. The values from ref. [48] cannot be used to predict changes in the EUV refractive index after optical or electronic excitation. Furthermore, they do not take into account the particular spatial structure of the vdW-HS. For example, possible differences in the refractive index between bulk material and monolayer material cannot be addressed. In addition to these concerns, the semiempirical values in ref. [48] have been found to be inaccurate even for standard materials.[51,52] For these reasons, we present ab initio calculations of the EUV refractive index for hBN and $MoTe_2$ and compare them to the values of ref. [48].

We restricted ourselves to comparing the in-plane refractive index (which corresponds to s-polarization in the XCT setup) for monolayer and bulk $MoTe_2$ and hBN in the spectral range from 25 to 55 eV. The ab initio calculations can be performed upto 50 eV and the data from ref. [48] is available from 30 eV on. The results are shown in **Figure 4**.

For both materials, discrepancies between the data from ref. [48], the results of ab initio calculations for the bulk material and the ab initio calculations for monolayers are evident. In $MoTe_2$ (see Figure 2a), the refractive index of the bulk crystal from ab initio calculations is close to the values of ref. [48] for high (>45 eV) photon energies. However, the ab initio calculations show a non-negligible difference between the bulk and monolayer refractive index over the entire spectral range. Furthermore, the tabulated values from ref. [48] are generally smoother than those obtained from our ab initio calculations. This can be ascribed to the structural and electronic details of the material that are intrinsically incorporated in the ab initio calculations. It is also worth noting that, in the imaginary part, the ab initio data feature the most intense resonance in the bulk at 40 eV, while this appears at about 43 eV in the tabulated values of ref. [48].

The lack of spectral features in the tabulated data from ref. [48] is even more evident in the case of hBN (see Figure 4b). Although the results of the ab initio calculations feature two absorption peaks at 25 and 36 eV both in the bulk and in the monolayer (although with significantly more intensity in the former), the reference from ref. [48] is given by a smooth and monotonically decreasing curve.

At the current state of development, the ab initio calculations cannot yet be performed for the entire EUV spectral range. In particular, the spectral range above 50 eV is not accessible where most XCT experiments on vdW-HS would be performed because the absorption in the bulk material decreases for high photon energies. Nevertheless, the ab initio calculations show that it is necessary to consider the effects of the electronic and structural details of the LMs, which are often neglected in the treatment of light-matter interaction in the EUV. In fact, the results suggest that XCT can actually be used to access the electronic properties in addition to the precise non-destructive characterization of the vdW-HS design.

3. Conclusion and Outlook

This work establishes optical coherence tomography with extreme ultraviolet light as a new method to investigate vdW-HS. We demonstrate this by studying a $MoTe_2$ monolayer encapsulated in hBN. Due to the small wavelength of the extreme ultraviolet light and the broad bandwidth used, we were able to reconstruct the axial structure of the sample with high accuracy in a nondestructive measurement. In particular, we precisely measured deviations in the thickness of the bulk layer, which is in good agreement with AFM measurements. Although AFM was used to verify the XCT results in this work, the two methods are complementary, especially because AFM is only surface sensitive, while XCT can provide depth information.

Furthermore, we calculate and measure the XCT contrast in different vdW-HS. We show that the available and commonly used refractive index database for the EUV spectral range[48] is incomplete and, in some cases, even inaccurate. Our ab initio calculations show inaccuracies of the standard database in the low-photon-energy region (below ≈45 eV), where first-principle modeling predicts pronounced absorption peaks.

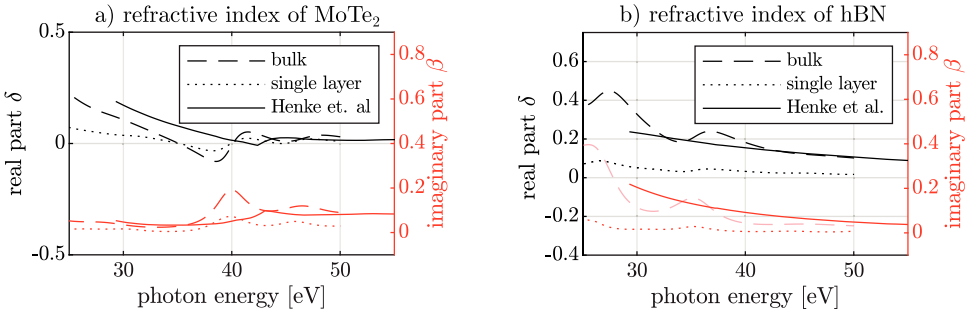

Figure 4. The real and imaginary parts of the refractive index tabulated in ref. [48] (solid line) is compared to the results from ab initio simulations for a) $MoTe_2$ and b) hBN in the bulk (dashed line) and single-layer form (dotted line).

In addition, the ab initio calculations exhibit differences between the refractive index for monolayer and bulk materials. The observed differences between the ab initio calculations and the calculations from atomic scattering factors of the elements are effects of the particular electronic and spatial structure of the LMs. This suggests that these effects can be directly investigated in future EUV imaging and spectroscopy experiments.

XCT is not restricted to the spectral range used in this work, and other wavelength regimes are accessible with high-harmonic generation. We envision that the spectral region for measurement can be optimized to maximize the XCT contrast or measure close to electronic transitions. For example, hBN has a transmission window between ≈200 and ≈400 eV, while carbon has an absorption edge at 282 eV. Consequently, this photon energy range is of high interest for the investigation of hBN-graphene vdW-HS. This largely coincides with the so-called water window, which has been a focus of the development in next-generation high-harmonic sources.[53–55]

In conclusion, this study provides the basis for EUV studies of interlayer effects in vdW-HS. Since the EUV light can be produced in the form of ultra-short pulses, our method potentially allows a direct and local measurement of ultrafast heat- and charge-transfer processes occurring at interfaces, with an unprecedented combination of axial and temporal resolution.

4. Experimental Section

EUV Coherence Tomography: The experiments were performed at a laser-based broadband EUV reflectometry beamline.[43,56] EUV radiation was produced by high-harmonic generation in argon. An infrared ultrashort laser pulse (pulse energy 2 mJ, pulse duration 35 fs, central wavelength 1300 nm, repetition rate 1 kHz) produced by a Ti:Sa laser system in combination with an optical parametric amplifier (OPA) was focused (focal length 30 cm) into a gas jet. The harmonics were emitted as comb spectra in the photon energy range of 30 – 100 eV. Thin metal filters were needed to separate the driving laser from the EUV radiation. In this work, zirconium filters were used that block infrared light and transmit EUV above ≈65 eV. If needed, a quasi-continuous EUV spectrum could be generated by shifting the harmonic combs within one illumination. This could be achieved by changing the center wavelength of the driving laser with the OPA.[57]

The divergent EUV radiation was focused with a toroidal mirror (focal length 1 m) on the sample. The focus size was ≈25 µm. The sample could be shifted relative to the EUV focus position to achieve lateral resolution. The reflected EUV was characterized by a custom-built spectrometer.[56] Referencing of the EUV flux incident on the sample could be achieved by recording the reflection of a reference sample before or after the measurement or by using the live-reference scheme described in ref. [51]. The Fourier transform of the sample reflectivity yielded the autocorrelation of the sample's axial structure. A 1D phase retrieval algorithm[22] could be used to recover the axial structure itself. However, in the case of trivial samples with a single encapsulated interface the autocorrelation could be used to interpret the sample structure.

Different modalities of the described setup have been used for the results shown in Figures 2 and 3. Due to the different shapes of the source spectrum and different reflectivity, contrast, or lateral dimensions of the sample, the measured spectral range, the referencing method, and the generation of quasi-continuous spectra were adopted. The experimental settings are summarized in **Table 1**.

Sample Preparation and Characterization: Double encapsulated monolayer flakes of 2H-$MoTe_2$ were fabricated by mechanical exfoliation of commercially available bulk crystals (HQ Graphene) using the polydimethylsiloxane (PDMS, GelPak) assisted dry transfer technique.[58] Since $MoTe_2$ flakes could undergo oxidation reactions[59,60] in ambient conditions, it was crucial that the bottom hBN flakes were transferred on the target substrate before exfoliation of $MoTe_2$ and the top hBN capping layer was transferred with minimal delay after $MoTe_2$ to prevent oxidation. The selected hBN flakes were mechanically exfoliated from high-quality crystals (NIMS, Japan) onto a silicon/silicon dioxide (Si/SiO_2) substrate with 300 nm oxide layer thickness, followed by exfoliation and dry-transfer of $MoTe_2$ from a PDMS stamp onto the as-transferred $hBN/Si/SiO_2$. The top hBN was transferred immediately after to minimize the exposure time of $MoTe_2$ to ambient conditions. In addition, it was stressed that exposure to air of $MoTe_2$ mainly affects its optical properties, while was not expected it to have a strong impact on its EUV response.

The hBN/graphene/hBN vdW-HS was prepared as for ref. [10].

The MoS_2 in SiO_2 sample was prepared by chemical vapor deposition (CVD) of MoS_2 on SiO_2, followed by physical vapor deposition (PVD) of SiO_2.

Table 1. Summary of the experimental settings for all measurements. The in situ reference refers to the scheme presented in ref. [51], ex situ is a reference measurement on a calibrated sample before or after the measurement.

Sample	Energy Range [eV]	Reference Method	Top bulk Thickness [nm]
hBN-$MoTe_2$	65–90	ex situ	140
$MoSe_2$-MoS_2	65–85	in situ	75, 100
SiO_2-MoS_2	65–90	in situ	60
hBN-C	68–100	ex situ	250

The $MoSe_2$-MoS_2-vdW-HS was produced by sequential transfer of $MoSe_2$ and MoS_2, which itself were produced by CVD.

AFM measurements were performed with a Veeco (formerly Digital Instruments) Nanoscope III AFM operated in the tapping mode using standard SiN tips. The used "J"-scanner was calibrated prior to the measurements by means of a HS-100MG height calibration standard from Budget-Sensors. This calibration sample itself had a height accuracy of 3%.

Contrast Simulation: The expected contrast of different sample structures was estimated by simulating the broadband sample reflectivity using the matrix method and tabulated atomic scattering factors.[48] The simulated samples were estimated with a monolayer encapsulated in two thicker layers of a different material (top thickness 80 nm, bottom thickness 120 nm) on a silicon substrate with 300 nm oxide layers. The sample reflectivity in the spectral region from E = 65 eV to E = 100 eV (corresponding to the transmission window of a Zr filter) was used for the XCT reconstruction.

XCT contrast was defined as the ratio between the signal at the depth of $z = 0$ and $z = 80$ nm. The XCT reconstruction was performed directly and without phase retrieval. Therefore, the reconstructed depth profile was the autocorrelation of the sample structure. As a consequence, the investigated contrast was a measure of the modulation amplitude in the reflected spectrum normalized to its offset.

For comparison of measured and expected contrasts, the samples were simulated with the structural parameters derived from the XCT measurement. In addition, the spectral range for each sample was adapted to the values used in the corresponding experiment.

Ab Initio Calculations: The ab initio calculations presented in this work were obtained in the framework of time-dependent density-functional theory[61] using the linear-response approach based on the Lanczos algorithm,[62] as implemented in Quantum ESPRESSO.[63] The Perdew–Burke–Ernzerhof functional[64] was adopted for the approximation of the exchange-correlation potential and augmented with the Tkatchenko–Scheffler scheme[65] to account for dispersive interlayer couplings. Optimized Norm-Conserving Vanderbilt pseudopotentials (SG15)[66] were employed to smooth out the electronic wave functions in the core region. A plane-wave basis set with kinetic energy and charge-density cutoff of 80 and 400 Ry, respectively, was adopted in all runs. A k-point mesh with 6 points in each periodic direction was used to sample the Brillouin zones.

Supporting Information

Supporting Information is available from the Wiley Online Library or from the author.

Acknowledgements

This work was supported by the German Research Foundation (grant numbers 390918228 and PA 730/13-1); European Social Fund (ESF) with Thüringer Aufbaubank (2018FGR008, 2015FGR0094), and Bundesministerium für Bildung und Forschung (VIP "X-CoherenT"). F.W., J.J.A., M.W., J.R., G.G.P., and S.F. acknowledge funding from the Helmholtz Institute Jena. F.W. is part of the Max Planck School of Photonics supported by BMBF, the Max Planck Society, and the Fraunhofer Society. J.P.G.F., A.M.V., and C.C. acknowledge funding from the German Research Foundation, Project No. 182087777 - CRC 951, from the German Federal Ministry of Education and Research (Professorinnenprogramm III) and from the State of Lower Saxony (Professorinnen für Niedersachsen, DyNano, SMART). Computational resources were provided by the high-performance computing cluster CARL at the University of Oldenburg, funded by the German Research Foundation (Project No. INST 184/157-1 FUGG) and by the Ministry of Science and Culture of Lower Saxony. G.S. acknowledges funding from the the German Research Foundation DFG (CRC 1375 NOA), project number 398816777 (subprojects B5 and C4). A.R.C. thanks the financial support the Brazilian National Council for Scientific and Technological Development (CNPq, project number 309920/2021-3). The authors thank Heiko Knopf for providing the SiO_2-MoS_2 sample. The authors thank Margarita Lapteva for her help with the sample preparation.

Conflict of Interest

The authors declare no conflict of interest.

Data Availability Statement

The data that support the findings of this study are available from the corresponding author upon reasonable request.

Keywords

DFT, extreme ultraviolet, EUV, layered heterostructures, optical coherence tomography

Received: July 11, 2024
Revised: August 22, 2024
Published online:

[1] M. Chhowalla, D. Jena, H. Zhang, *Nat. Rev. Mater.* **2016**, *1*, 1.
[2] K. F. Mak, J. Shan, D. C. Ralph, *Nat. Rev. Phys.* **2019**, *1*, 646.
[3] Y. Li, N. An, Z. Lu, Y. Wang, B. Chang, T. Tan, X. Guo, X. Xu, J. He, H. Xia, Z. Wu, Y. Su, Y. Liu, Y. Rao, G. Soavi, B. Yao, *Nat. Commun.* **2022**, *13*, 1.
[4] T. Boolakee, C. Heide, A. Garzón-Ramírez, H. B. Weber, I. Franco, P. Hommelhoff, *Nature* **2022**, *605*, 251.
[5] J. He, I. Paradisanos, T. Liu, A. R. Cadore, J. Liu, M. Churaev, R. N. Wang, A. S. Raja, C. Javerzac-Galy, P. Roelli, D. D. Fazio, B. L. Rosa, S. Tongay, G. Soavi, A. C. Ferrari, T. J. Kippenberg, *Nano Lett.* **2021**, *21*, 2709.
[6] J. S. Ross, P. Klement, A. M. Jones, N. J. Ghimire, J. Yan, D. Mandrus, T. Taniguchi, K. Watanabe, K. Kitamura, W. Yao, D. H. Cobden, X. Xu, *Nat. Nanotechnol.* **2014**, *9*, 268.
[7] F. Xia, T. Mueller, Y.-m. Lin, A. Valdes-Garcia, P. Avouris, *Nat. Nanotechnol.* **2009**, *4*, 839.
[8] Y. Liu, N. O. Weiss, X. Duan, H.-C. Cheng, Y. Huang, X. Duan, *Nat. Rev. Mater.* **2016**, *1*, 1.
[9] L. Banszerus, H. Janssen, M. Otto, A. Epping, T. Taniguchi, K. Watanabe, B. Beschoten, D. Neumaier, C. Stampfer, *2D Mater.* **2017**, *4*, 025030.
[10] L. Viti, A. R. Cadore, X. Yang, A. Vorobiev, J. E. Muench, K. Watanabe, T. Taniguchi, J. Stake, A. C. Ferrari, M. S. Vitiello, *Nanophotonics* **2020**, *10*, 89.
[11] Y. Cao, V. Fatemi, S. Fang, K. Watanabe, T. Taniguchi, E. Kaxiras, P. Jarillo-Herrero, *Nature* **2018**, *556*, 43.
[12] C. Jin, E. C. Regan, A. Yan, M. Iqbal Bakti Utama, D. Wang, S. Zhao, Y. Qin, S. Yang, Z. Zheng, S. Shi, K. Watanabe, T. Taniguchi, S. Tongay, A. Zettl, F. Wang, *Nature* **2019**, *567*, 76.
[13] K. K. Paul, J.-H. Kim, Y. H. Lee, *Nat. Rev. Phys.* **2021**, *3*, 178.
[14] K.-J. Tielrooij, N. C. Hesp, A. Principi, M. B. Lundeberg, E. A. Pogna, L. Banszerus, Z. Mics, M. Massicotte, P. Schmidt, D. Davydovskaya, D. G. Purdie, I. Goykhman, G. Soavi, A. Lombardo, K. Watanabe, T. Taniguchi, M. Bonn, D. Turchinovich, C. Stampfer, A. C. Ferrari, G. Cerullo, M. Polini, F. H. L. Koppens, *Nat. Nanotechnol.* **2018**, *13*, 41.
[15] A. C. Ferrari, D. M. Basko, *Nature Nanotech.* **2013**, *8*, 235.
[16] A. C. Ferrari, J. C. Meyer, V. Scardaci, C. Casiraghi, M. Lazzeri, F. Mauri, S. Piscanec, D. Jiang, K. S. Novoselov, S. Roth, A. K. Geim, *Phys. Rev. Lett.* **2006**, *97*, 187401.
[17] D. Saleta Reig, S. Varghese, R. Farris, A. Block, J. D. Mehew, O. Hellman, P. Woźniak, M. Sledzinska, A. El Sachat, E. Chávez-Ángel, S. O. Valenzuela, N. F. van Hulst, P. Ordejón, Z. Zanolli, C. M. S. Torres, M. J. Verstraete, *Adv. Mater.* **2022**, *34*, 2108352.

[18] E. Simsek, B. Mukherjee, *Nanotechnology* **2015**, *26*, 455701.
[19] O. Dogadov, C. Trovatello, B. Yao, G. Soavi, G. Cerullo, *Laser Photonics Rev.* **2022**, *16*, 2100726.
[20] M. Massicotte, P. Schmidt, F. Vialla, K. Watanabe, T. Taniguchi, K.-J. Tielrooij, F. H. Koppens, *Nat. Commun.* **2016**, *7*, 12174.
[21] C. Nyby, A. Sood, P. Zalden, A. J. Gabourie, P. Muscher, D. Rhodes, E. Mannebach, J. Corbett, A. Mehta, E. Pop, T. F. Heinz, A. M. Lindenberg, *Adv. Funct. Mater.* **2020**, *30*, 2002282.
[22] S. Fuchs, M. Wünsche, J. Nathanael, J. J. Abel, C. Rödel, J. Biedermann, J. Reinhard, U. Hübner, G. G. Paulus, *Optica* **2017**, *4*, 903.
[23] P. Wachulak, A. Bartnik, H. Fiedorowicz, *Sci. Rep.* **2018**, *8*, 8494.
[24] F. Wiesner, M. Wünsche, J. Reinhard, J. J. Abel, J. Nathanael, S. Skruszewicz, C. Rödel, S. Yulin, A. Gawlik, G. Schmidl, U. Hübner, J. Plentz, G. G Paulus, S. Fuchs, *Optica* **2021**, *8*, 230.
[25] M. Chergui, M. Beye, S. Mukamel, C. Svetina, C. Masciovecchio, *Nat. Rev. Phys.* **2023**, 1.
[26] S. Biswas, L. R. Baker, *Acc. Chem. Res.* **2022**, *55*, 893.
[27] M. Ferray, A. L'Huillier, X. F. Li, L. A. Lompre, G. Mainfray, C. Manus, *J. Phys. B: At., Mol. Opt. Phys.* **1988**, *21*, 31.
[28] A. McPherson, G. Gibson, H. Jara, U. Johann, T. S. Luk, I. McIntyre, K. Boyer, C. K. Rhodes, *JOSA B* **1987**, *4*, 595.
[29] M. Lewenstein, P. Balcou, M. Y. Ivanov, A. L'huillier, P. B. Corkum, *Phys. Rev. A* **1994**, *49*, 2117.
[30] P. á. Corkum, F. Krausz, *Nat. Phys.* **2007**, *3*, 381.
[31] C. J. Kaplan, P. M. Kraus, A. D. Ross, M. Zürch, S. K. Cushing, M. F. Jager, H.-T. Chang, E. M. Gullikson, D. M. Neumark, S. R. Leone, *Phys. Rev. B* **2018**, *97*, 205202.
[32] M. Schultze, E. M. Bothschafter, A. Sommer, S. Holzner, W. Schweinberger, M. Fiess, M. Hofstetter, R. Kienberger, V. Apalkov, V. S. Yakovlev, M. I. Stockman, F. Krausz, *Nature* **2013**, *493*, 75.
[33] M. Schultze, K. Ramasesha, C. Pemmaraju, S. Sato, D. Whitmore, A. Gandman, J. S. Prell, L. Borja, D. Prendergast, K. Yabana, D. M. Neumark, S. R. Leone, *Science* **2014**, *346*, 1348.
[34] J. Rothhardt, G. K. Tadesse, W. Eschen, J. Limpert, *J. Opt.* **2018**, *20*, 113001.
[35] H. N. Chapman, K. A. Nugent, *Nat. Photonics* **2010**, *4*, 833.
[36] M. Zürch, J. Rothhardt, S. Hädrich, S. Demmler, M. Krebs, J. Limpert, A. Tünnermann, A. Guggenmos, U. Kleineberg, C. Spielmann, *Sci. Rep.* **2014**, *4*, 7356.
[37] S. Witte, V. T. Tenner, D. W. Noom, K. S. Eikema, *Light: Sci. Appl.* **2014**, *3*, e163.
[38] J. Reinhard, S. Kaleta, J. J. Abel, F. Wiesner, M. Wünsche, E. Seemann, M. Westermann, T. Weber, J. Nathanael, A. Iliou, H. Fiedorowicz, F. Hillmann, C. Eggeling, G. G. Paulus, S. Fuchs, *Microsc. Microanal.* **2023**, ozad123.
[39] G. K. Tadesse, W. Eschen, R. Klas, M. Tschernajew, F. Tuitje, M. Steinert, M. Zilk, V. Schuster, M. Zürch, T. Pertsch, C. Spielmann, J. Limpert, J. Rothhardt, *Sci. Rep.* **2019**, *9*, 1.
[40] D. F. Gardner, M. Tanksalvala, E. R. Shanblatt, X. Zhang, B. R. Galloway, C. L. Porter, R. Karl, C. Bevis, D. E. Adams, H. C. Kapteyn, M. M. Murnane, G. F. Mancini, *Nat. Photonics* **2017**, *11*, 259.
[41] M. Tanksalvala, C. L. Porter, Y. Esashi, B. Wang, N. W. Jenkins, Z. Zhang, G. P. Miley, J. L. Knobloch, B. McBennett, N. Horiguchi, S. Yazdi, J. Zhou, M. N. Jacobs, C. S. Bevis, R. M. KarlJr., P. Johnsen, D. Ren, L. Waller, D. E. Adams, S. L. Cousin, C.-T. Liao, J. Miao, M. Gerrity, H. C. Kapteyn, M. M. Murnane, *Sci. Adv.* **2021**, *7*, eabd9667.
[42] F. Wiesner, S. Skruszewicz, C. Rödel, J. J. Abel, J. Reinhard, M. Wünsche, J. Nathanael, M. Grünewald, U. Hübner, G. G. Paulus, S. Fuchs, *Opt. Express* **2022**, *30*, 32267.
[43] J. Nathanael, M. Wünsche, S. Fuchs, T. Weber, J. J. Abel, J. Reinhard, F. Wiesner, U. Hübner, S. J. Skruszewicz, G. G. Paulus, C. Rödel, *Rev. Sci. Instrum.* **2019**, *90*, 11.
[44] L. Drescher, O. Kornilov, T. Witting, G. Reitsma, N. Monserud, A. Rouzée, J. Mikosch, M. J. Vrakking, B. Schütte, *Nature* **2018**, *564*, 91.
[45] J. Yamada, S. Matsuyama, I. Inoue, T. Osaka, T. Inoue, N. Nakamura, Y. Tanaka, Y. Inubushi, T. Yabuuchi, K. Tono, K. Tamasaku, H. Yumoto, T. Koyama, H. Ohashi, M. Yabashi, K. Yamauchi, *Nat. Photonics* **2024**, 1.
[46] C. Xu, H. W. Yong, J. He, R. Long, A. R. Cadore, I. Paradisanos, A. K. Ott, G. Soavi, S. Tongay, G. Cerullo, A. C. Ferrari, O. V. Prezhdo, Z.-H. Loh, *ACS Nano* **2020**, *15*, 819.
[47] C. Ruppert, B. Aslan, T. F. Heinz, *Nano Lett.* **2014**, *14*, 6231.
[48] B. L. Henke, E. M. Gullikson, J. C. Davis, *At. Data Nucl. Data Tables* **1993**, *54*, 181.
[49] Y. Esashi, M. Tanksalvala, Z. Zhang, N. W. Jenkins, H. C. Kapteyn, M. M. Murnane, *OSA Continuum* **2021**, *4*, 1497.
[50] J. J. Abel, J. Apell, F. Wiesner, J. Reinhard, M. Wünsche, N. Felde, G. Schmidl, J. Plentz, G. G. Paulus, S. Lippmann, S. Fuchs, *Mater. Charact.* **2024**, *211*, 113894.
[51] J. J. Abel, F. Wiesner, J. Nathanael, J. Reinhard, M. Wünsche, G. Schmidl, A. Gawlik, U. Hübner, J. Plentz, C. Rödel, G. G Paulus, S. Fuchs, *Opt. Express* **2022**, *30*, 35671.
[52] R. Ciesielski, Q. Saadeh, V. Philipsen, K. Opsomer, J.-P. Soulié, M. Wu, P. Naujok, R. W. van de Kruijs, C. Detavernier, M. Kolbe, F. Scholze, V. Soltwisch, *Appl. Opt.* **2022**, *61*, 2060.
[53] J. Pupeikis, P.-A. Chevreuil, N. Bigler, L. Gallmann, C. R. Phillips, U. Keller, *Optica* **2020**, *7*, 168.
[54] M. Gebhardt, T. Heuermann, R. Klas, C. Liu, A. Kirsche, M. Lenski, Z. Wang, C. Gaida, J. E. Antonio-Lopez, A. Schülzgen, R. Amezcua-Correa, J. Rothhardt, J. Limpert, *Light: Sci. Appl.* **2021**, *10*, 2047.
[55] T. Feng, A. Heilmann, M. Bock, L. Ehrentraut, T. Witting, H. Yu, H. Stiel, S. Eisebitt, M. Schnürer, *Opt. Express* **2020**, *28*, 8724.
[56] M. Wünsche, S. Fuchs, T. Weber, J. Nathanael, J. J. Abel, J. Reinhard, F. Wiesner, U. Hübner, S. J. Skruszewicz, G. G. Paulus, C. Rödel, *Rev. Sci. Instrum.* **2019**, *90*, 2.
[57] M. Wünsche, S. Fuchs, S. Aull, J. Nathanael, M. Möller, C. Rödel, G. G. Paulus, *Opt. Express* **2017**, *25*, 6936.
[58] R. Frisenda, E. Navarro-Moratalla, P. Gant, D. P. De Lara, P. Jarillo-Herrero, R. V. Gorbachev, A. Castellanos-Gomez, *Chem. Soc. Rev.* **2018**, *47*, 53.
[59] B. Chen, H. Sahin, A. Suslu, L. Ding, M. I. Bertoni, F. M. Peeters, S. Tongay, *ACS Nano* **2015**, *9*, 5326.
[60] G. Mirabelli, C. McGeough, M. Schmidt, E. K. McCarthy, S. Monaghan, I. M. Povey, M. McCarthy, F. Gity, R. Nagle, G. Hughes, A. Cafolla, P. K. Hurley, R. Duffy, *J. Appl. Phys.* **2016**, *120*, 12.
[61] E. Runge, E. K. Gross, *Phys. Rev. Lett.* **1984**, *52*, 997.
[62] O. B. Malcıoğlu, R. Gebauer, D. Rocca, S. Baroni, *Comput. Phys. Commun.* **2011**, *182*, 1744.
[63] P. Giannozzi, O. Andreussi, T. Brumme, O. Bunau, M. B. Nardelli, M. Calandra, R. Car, C. Cavazzoni, D. Ceresoli, M. Cococcioni, N. Colonna, I. Carnimeo, A. D. Corso, S. de Gironcoli, P. Delugas, R. A. DiStasio, A. Ferretti, A. Floris, G. Fratesi, G. Fugallo, R. Gebauer, U. Gerstmann, F. Giustino, T. Gorni, J. Jia, M. Kawamura, H.-Y. Ko, A. Kokalj, E. Küçükbenli, M. Lazzeri, et al., *J. Phys.: Consdes. Matter* **2017**, *29*, 465901.
[64] J. P. Perdew, K. Burke, M. Ernzerhof, *Phys. Rev. Lett.* **1996**, *77*, 3865.
[65] A. Tkatchenko, M. Scheffler, *Phys. Rev. Lett.* **2009**, *102*, 073005.
[66] D. R. Hamann, *Phys. Rev. B* **2013**, *88*, 085117.